Article

Synthesis and Characterization of $Bi_2W_xMo_{1-x}O_6$ Solid Solutions and Their Application in Photocatalytic Desulfurization under Visible Light

Artem S. Belousov *, Evgeny V. Suleimanov, Alina A. Parkhacheva, Diana G. Fukina, Andrey V. Koryagin, Dmitry N. Titaev and Mikhail A. Lazarev

Research Institute for Chemistry, Lobachevsky State University of Nizhny Novgorod, 603950 Nizhny Novgorod, Russia; suev@mail.ru (E.V.S.); alinaparhaceva64802@gmail.com (A.A.P.); dianafuk@yandex.ru (D.G.F.); kor-andrey14@yandex.ru (A.V.K.); dmitriy151@yandex.ru (D.N.T.); lazarev@ichem.unn.ru (M.A.L.)
* Correspondence: belousov@ichem.unn.ru

Abstract: Photocatalytic oxidative desulfurization has attracted much attention in recent years due to the continuous tightening of the sulfur content requirements in motor fuels and the disadvantages of the industrial hydrodesulfurization process. This work is devoted to the investigation of the photocatalytic activity of $Bi_2W_xMo_{1-x}O_6$ solid solutions (x = 1, 0.75, 0.5, 0.25, 0) in the oxidative desulfurization of hydrocarbons under visible light irradiation using hydrogen peroxide as an oxidant. The synthesized photocatalysts were characterized in detail using XRD, SEM, EDS, low-temperature nitrogen adsorption–desorption, and DRS. It was shown that the use of solid solutions $Bi_2W_xMo_{1-x}O_6$ with x = 0.5–0.75 leads to the complete oxidation of organosulfur compounds to CO_2 and H_2O within 120 min. The high photocatalytic activity of solid solutions (x = 0.5–0.75) is attributed to their ability to absorb more visible light, the presence of the corner-shared $[Mo/WO_6]$ octahedral layers, which may promote the generation and separation of photogenerated charges, and the hierarchical 3D flower-like structure. The reaction mechanism of the desulfurization was also analyzed in this work.

Keywords: semiconductors; layered perovskites; photocatalysis; desulfurization; visible light

1. Introduction

Nowadays, an important direction is the development of highly active heterogeneous photocatalysts for industrially important processes, such as water and air purification, hydrogen evolution, the oxidation of organic substrates, and the reduction of carbon dioxide [1]. In recent years, there has also been a growing interest in the photocatalytic oxidative desulfurization (PODS) of liquid hydrocarbons [2,3]. This fact can be explained by the continuous tightening of the sulfur content requirements in motor fuels and the disadvantages of the industrial hydrodesulfurization process, namely harsh reaction conditions, the rapid deactivation of catalysts, and their low activity towards large sulfur-containing molecules, e.g., dibenzothiophene (DBT).

The most common types of semiconductors used in various photocatalytic reactions are inexpensive and naturally abundant transition metal oxides, especially titanium dioxide (TiO_2). The extensive use of this material is also associated with its low toxicity, high efficiency, and stability [4,5]. The most significant limitation of TiO_2 is its large band gap (E_g = 3.0–3.4 eV), which makes it possible to use only the ultraviolet (UV) region to initiate photocatalytic processes [6]. In the field of the development of photocatalysts for PODS, the shifting sensitivity of TiO_2 to the visible region by its modification remains the most common approach. The main strategies are photosensitization using metal nanoparticles,

for example, Ag [7], the creation of heterojunctions [8,9], and band gap engineering, namely the doping of TiO_2 with nitrogen or sulfur into anionic positions [10,11].

In the wide range of numerous visible light-responsive metal oxide semiconductors, bismuth tungstate (Bi_2WO_6), which belongs to the Aurivillius family of layered perovskites with the general formula $Bi_2A_{n-1}B_nO_{3n+3}$, has received significant attention in recent years for the photocatalytic removal of organic pollutants from wastewater [12,13], water splitting [14], and CO_2 reduction [15]. The main advantages of Bi-containing layered perovskites are their intense absorption of visible light, high photocatalytic activity, ease of preparation, and ability to control properties by varying their composition and synthesis conditions [16,17].

It has recently been demonstrated that composite materials based on bismuth tungstate Bi_2WO_6 exhibit a relatively high activity in PODS under visible light irradiation [18–20]. Wu et al. [18] found that the Nb_2O_5/Bi_2WO_6 exhibited a considerably higher activity than pure Nb_2O_5 and Bi_2WO_6 and the desulfurization rate achieved 99% after visible light irradiation for 120 min. These results could be explained by the formation of a heterojunction and, accordingly, the effective separation of photogenerated electron–hole pairs on the Nb_2O_5-Bi_2WO_6 hybrid. A similar effect was obtained on the NiO-Bi_2WO_6 heterojunction in the photocatalytic oxidation of benzothiophene [20]. Li and co-workers [21] investigated the photocatalytic activity of $Bi_2W_{1-x}Mo_xO_6$/montmorillonite in the oxidation of DBT using H_2O_2 as an oxidant. The authors demonstrated that the incorporation of Mo atoms into the Bi_2WO_6 structure significantly improved the photocatalytic activity of composites. On the other hand, the effect of physicochemical properties (specific surface area, morphology, optical properties, etc.) of unmodified $Bi_2W_{1-x}Mo_xO_6$ photocatalysts on their performances in PODS remains unknown.

Herein, we report the preparation of $Bi_2W_xMo_{1-x}O_6$ (x = 1, 0.75, 0.5, 0.25, 0) layered perovskites by a hydrothermal route and their photocatalytic activity in PODS under visible light irradiation using H_2O_2 as an oxidant. All the synthesized samples were characterized by X-ray diffraction analysis (XRD), scanning electron microscopy (SEM), energy-dispersive X-ray spectroscopy (EDS), low-temperature nitrogen adsorption–desorption, and UV-Vis diffuse reflectance spectroscopy (DRS). The analysis of the effect of the physicochemical properties of $Bi_2W_xMo_{1-x}O_6$ photocatalysts with different Mo and W content on their activity in PODS was performed in detail.

2. Materials and Methods

2.1. Preparation of $Bi_2W_xMo_{1-x}O_6$ Solid Solutions

The synthesis of $Bi_2W_xMo_{1-x}O_6$ (x = 0, 0.25, 0.50, 0.75, 1) layered perovskites was conducted by a hydrothermal route using $Bi(NO_3)_3\cdot5H_2O$ (99%), $Na_2WO_4\cdot2H_2O$ (99%), and $Na_2MoO_4\cdot2H_2O$ (99%) as starting materials. The starting materials for the synthesis of perovskites were preliminarily stirred in 30 mL of distilled water for 1 h, then transferred into a 50 mL Teflon-lined stainless-steel autoclave and treated at 160 °C for 12 h. The preparation conditions for $Bi_2W_xMo_{1-x}O_6$ (x = 0, 0.25, 0.50, 0.75, 1) layered perovskites are listed in Table 1.

Table 1. Hydrothermal synthesis of $Bi_2W_xMo_{1-x}O_6$ perovskites.

x	Perovskite	Molar Ratio of Starting Materials	Temperature and Holding Time
1	Bi_2WO_6	Na_2WO_4:$Bi(NO_3)_3$ = 1:2	160 °C, 12 h
0.75	$Bi_2W_{0.75}Mo_{0.25}O_6$	Na_2WO_4:Na_2MoO_4:$Bi(NO_3)_3$ = 1.5:0.5:4	160 °C, 12 h
0.5	$Bi_2W_{0.5}Mo_{0.5}O_6$	Na_2WO_4:Na_2MoO_4:$Bi(NO_3)_3$ = 1:1:4	160 °C, 12 h
0.25	$Bi_2W_{0.25}Mo_{0.75}O_6$	Na_2WO_4:Na_2MoO_4:$Bi(NO_3)_3$ = 0.5:1.5:4	160 °C, 12 h
0	Bi_2MoO_6	Na_2MoO_4:$Bi(NO_3)_3$ = 1:2	160 °C, 12 h

2.2. Characterization

XRD patterns were recorded on a Shimadzu XRD-6100 diffractometer (CuKα radiation λ = 1.5418 Å) with a Ni filter (2θ = 10–80°, 2°·min^{-1}). The mean crystallite size D (nm) of $Bi_2W_xMo_{1-x}O_6$ layered perovskites was determined from the full width at half-maximum (FWMH) of the corresponding diffraction peaks by using the Scherrer equation:

$$D = \frac{K\lambda}{\beta \cos\theta}$$ (1)

where K is the shape factor (0.94), λ is the X-ray wavelength (1.5418 nm in our case), β is the line broadening at FWHM in radians, and θ is the Bragg angle.

The morphology of the prepared photocatalysts was studied by SEM on a JSM-IT300LV microscope (JEOL, Welwyn Garden City, UK). The elemental composition was proved by energy dispersive X-ray spectroscopy (EDS) equipped with an X-max^N 20 detector (Oxford Instruments, Shanghai, China).

The specific surface areas of $Bi_2W_xMo_{1-x}O_6$ layered perovskites were determined from the low-temperature N_2 adsorption–desorption using an Autosorb iQ-C apparatus (Quantachrome Instruments, Boynton Beach, FL 33426, USA). Before measurements, the samples were degassed under a dynamic vacuum condition (base pressure = 1.33×10^{-4} Pa) at 120 °C for 3 h. Nitrogen (N_2) was used as an adsorptive gas for the adsorption–desorption isotherm measurements. The specific surface area of the photocatalysts was estimated by the Brunauer–Emmett–Teller (BET) method using data taken in the range of $0.05 < p/p_0 < 0.35$.

UV-Vis diffuse reflectance spectra were obtained on a Cary 5000 spectrophotometer (Varian, New York, NY, USA). The optical band gaps (E_g) of the as-prepared materials were determined using the Kubelka–Munk theory by the following equation:

$$F(R_\infty) = \frac{(1 - R_\infty)^2}{2R_\infty} = \frac{\alpha}{s}$$ (2)

where R_∞ is the relative diffuse reflectance, α is the absorption coefficient, and s is the scattering coefficient.

The Kubelka–Munk function $F(R_\infty)$ is proportionate to the absorption coefficient α if the scattering coefficient is independent of the wavelength. The Tauc method [22] was used for the determination of the E_g of the semiconductors:

$$(F(R_\infty)h\nu)^2 = C(h\nu - E_g)$$ (3)

where ν is the frequency, h is the Plank constant, and C is the proportional coefficient.

2.3. Photocatalytic Oxidative Desulfurization

Model fuel with a sulfur concentration of 200 ppm was prepared by dissolving 0.0863 g of DBT in 100 mL of *n*-dodecane. PODS experiments were operated in a beaker with magnetic stirring at ambient temperature. A 30 W LED lamp (6500 K, λ = 420–600 nm) was used as the visible light source. The distance from the light source to the model fuel was about 10 cm.

Typically, 10 mL of model fuel was firstly added into a 100 mL beaker, and then photocatalyst (0.1 g) and H_2O_2 (30 wt%, H_2O_2/DBT molar ratio of 10) were also introduced in order. The beaker was placed in the dark with constant magnetic stirring for 30 min to establish an adsorption–desorption equilibrium. Then, the PODS experiments were carried out under visible light irradiation for 120 min. Samples were taken every 20 min. The photocatalyst powder was separated from the reaction mixture by centrifugation.

The analysis of the reaction mixture before and after photocatalysis was carried out on a gas chromatograph Shimadzu GC-2010 Plus equipped with a flame ionization detector and a ZB-FFAP capillary column (length of 50 m; inner diameter of 0.32 mm; film thickness

of 0.50 µm). Helium was used as a carrier gas. The desulfurization degree was calculated by the following equation:

$$X = ((C_0 - C)/C_0) \times 100\% \tag{4}$$

where C_0 (ppm) is the initial sulfur concentration and C (ppm) is the sulfur concentration within a certain period of time.

The main oxidation products were detected using a gas chromatography-mass spectrometer (GC-MS) Shimadzu QP-2010 equipped with an Equity-5 capillary column (length of 30 m; inner diameter of 0.32 mm; film thickness of 0.25 µm). Helium was used as a carrier gas.

2.4. Active Species Trapping Experiments

In order to establish the active species formed during the reaction and the mechanism of PODS, active radical trapping experiments were carried out. In these experiments, isopropanol (IPA), benzoquinone (BQ), and EDTA-2Na were used as radical scavengers for hydroxyl radicals ($^\bullet$OH), superoxide ($O_2^{\bullet-}$), and holes (h^+), respectively.

2.5. Stability Test

For the investigation of stability, the photocatalyst after PODS was separated from the reaction mixture by the centrifugation, washed with ethanol and distilled water, dried at 80 °C for 12 h, and then directly used for the next run.

3. Results and Discussion

3.1. XRD Analysis

Figure 1 represents the XRD patterns of the $Bi_2W_xMo_{1-x}O_6$ layered perovskites. As can be seen, the characteristic peaks are detected at 28.4°, 32.9°, 47.2°, 55.9°, 58.6°, and 76.0°, corresponding to the (113), (200), (220), (313), (226), and (139) crystal planes of Bi_2WO_6 with $x = 1$ (JCPDS No. 39-0256) [23,24], respectively. No other diffraction peaks were detected, indicating the high purity of the sample. For $x = 0$, high-purity orthorhombic Bi_2MoO_6, the so-called γ-Bi_2MoO_6 phase (JCPDS No. 21-0102) [25], was obtained. It can also be found from Figure 1 that with an increase of the Mo content in the photocatalyst, the intensity of the (002) diffraction peak, which is characteristic for Bi_2MoO_6, increases compared to the most intense peak (113). At the same time, the narrowing of the (113) diffraction peak was observed, which indicates an increase of the average crystallite size (Table 2) from 13.02 nm for Bi_2WO_6 ($x = 1$) to 28.38 nm for Bi_2MoO_6 ($x = 0$). The higher crystallinity of the compounds with a high content of Mo could be explained by the lower crystallization temperature of γ-Bi_2MoO_6 compared to Bi_2WO_6 [26].

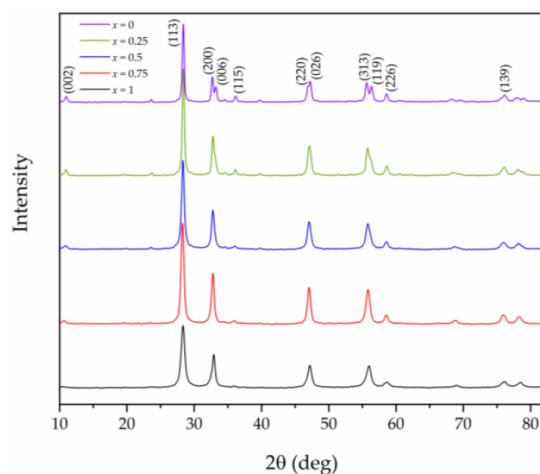**Figure 1.** XRD patterns of as-prepared $Bi_2W_xMo_{1-x}O_6$ perovskites.

Table 2. Lattice parameters and physicochemical properties of $Bi_2W_xMo_{1-x}O_6$ layered perovskites.

x	a (Å)	b (Å)	c (Å)	V (Å^3)	D_{113} (nm)	D_{002} (nm)	S_{BET} (m$^2\cdot$g^{-1})	E_g (eV)
1	5.446 (2)	5.458 (9)	16.36 (1)	486.7 (7)	13.02	-	25.8	2.90
0.75	5.468 (4)	5.446 (2)	16.39 (5)	487.9 (7)	17.18	-	19.3	2.63
0.5	5.455 (3)	5.461 (1)	16.37 (6)	487.6 (3)	17.96	13.28	16.4	2.60
0.25	5.449 (6)	5.468 (7)	16.34 (1)	486.8 (5)	24.28	20.70	14.8	2.65
0	5.471 (3)	5.480 (6)	16.25 (1)	487.3 (3)	28.38	21.81	15.3	2.68

3.2. Morphology

The SEM images of the as-prepared photocatalysts $Bi_2W_xMo_{1-x}O_6$ are shown in Figure 2. Layered perovskite Bi_2WO_6 ($x = 1$) has a 3D flower-like structure, consisting of nanosheets with widths of 50–80 nm, while Bi_2MoO_6 ($x = 0$) is composed from irregularly shaped nanosheets with widths of 100–300 nm, which form agglomerates up to 5 μm. Interestingly, at a high W content in the $Bi_2W_xMo_{1-x}O_6$ structure, the 3D flower-like morphology is retained, but at $x < 0.5$ the destruction of the flowers with the formation of individual nanosheets occurs.
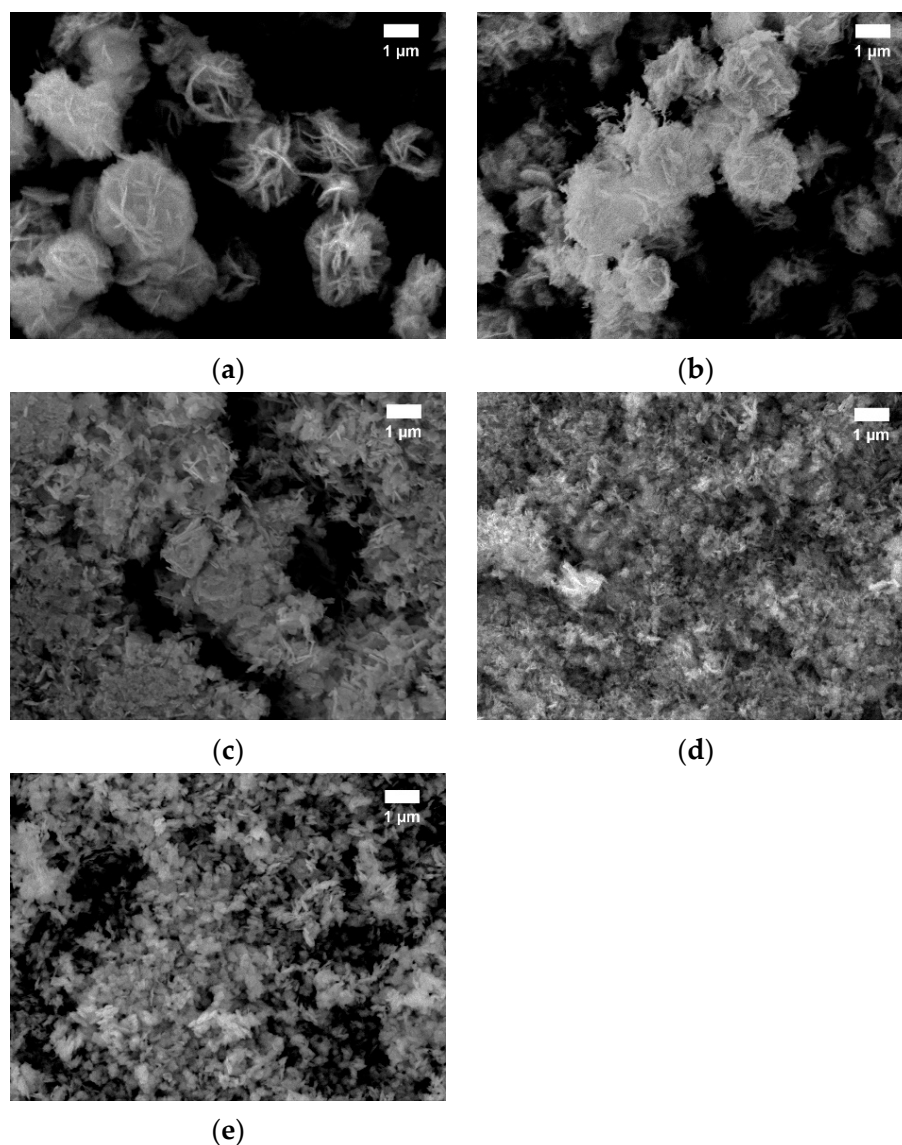

(a)

(b)

(c)

(d)

(e)

Figure 2. SEM images for $Bi_2W_xMo_{1-x}O_6$ layered perovskites: (**a**) $x = 1$; (**b**) $x = 0.75$; (**c**) $x = 0.5$; (**d**) $x = 0.25$; (**e**) $x = 0$.

The study of the elemental composition of the obtained samples also confirmed the formation of solid solutions with a given composition within the sensitivity of the method (~1–3 at%). Elemental mapping showed a uniform distribution of Bi (Mα), W (Lα), Mo (Lα), and O (Kα) throughout the samples (Table 3). According to EDS, the actual chemical formulas of the solid solutions, where x = 0.75, 0.5, and 0.25, should be written as $Bi_2W_{0.78}Mo_{0.22}O_6$, $Bi_2W_{0.53}Mo_{0.47}O_6$, and $Bi_2W_{0.24}Mo_{0.76}O_6$, respectively.

Table 3. Elemental composition of layered perovskites $Bi_2W_xMo_{1-x}O_6$ (at%) obtained from EDS.

x	Perovskite	Bi	W	Mo	O
1	Bi_2WO_6	20.96	11.94	-	67.10
0.75	$Bi_2W_{0.75}Mo_{0.25}O_6$	22.13	8.82	2.59	65.42
0.5	$Bi_2W_{0.5}Mo_{0.5}O_6$	20.93	6.11	5.55	67.22
0.25	$Bi_2W_{0.25}Mo_{0.75}O_6$	21.56	2.79	7.75	65.90
0	Bi_2MoO_6	21.15	-	11.35	67.50

3.3. UV-Vis Analysis and Electronic Structure

The UV-Vis spectra of the $Bi_2W_xMo_{1-x}O_6$ compounds (Figure 3a) showed that these materials have an intense absorption ability towards visible light ($\lambda \geq 420$ nm). We detected a significant red shift when the Mo atoms were introduced into the crystal lattice of Bi_2WO_6, which indicates a decrease of E_g for the compounds with $x \leq 0.75$. For instance, if Bi_2WO_6 has an E_g of 2.90 eV, then Mo-containing perovskites have band gaps in the range of 2.60–2.70 eV (Table 2, Figure 3b).
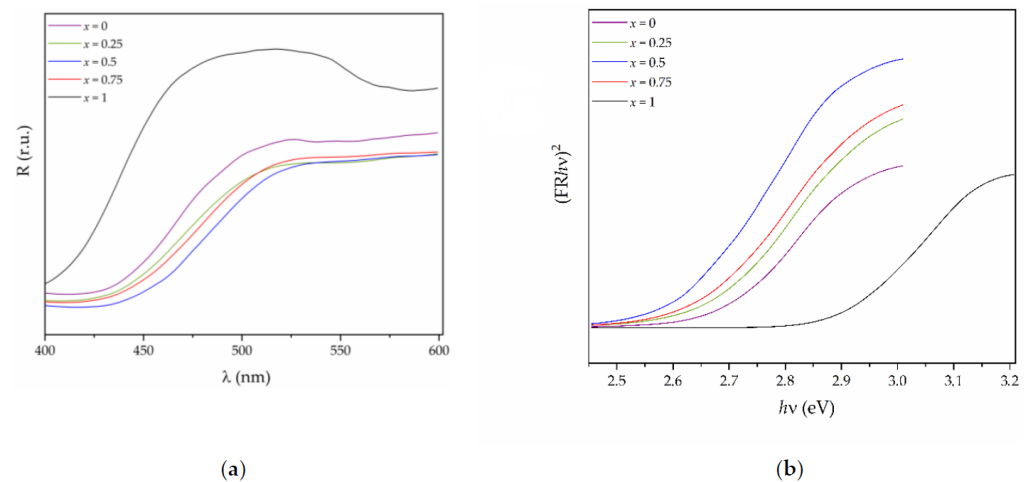

Figure 3. (**a**) UV-Vis spectra and (**b**) Tauc plots for $Bi_2W_xMo_{1-x}O_6$ layered perovskites.

It is well-known that the conduction band (CB) and valence band (VB) edge potentials of a solid material play a crucial role in the photocatalysis. The edge potentials of semiconductors can be estimated according to the following equations [27]:

$$E_{VB} = \chi - E_C + 0.5E_g \tag{5}$$

$$E_{CB} = E_{VB} - E_g \tag{6}$$

where E_{CB} and E_{VB} are the conduction and valence band potentials, respectively, χ is the Mulliken electronegativity of a semiconductor [28,29], E_C is the free electron energy with respect to a normal hydrogen electrode (4.5 eV), and E_g is the band gap energy.

The Mulliken electronegativity of compounds $A_aB_bC_c$ can be calculated by the following equation [30,31]:

$$\chi(A_aB_bC_c) = (\chi(A)^a\chi(B)^b\chi(C)^c)^{1/(a+b+c)} \tag{7}$$

where $\chi(A)$, $\chi(B)$, and $\chi(C)$ are the absolute electronegativity of the A atoms, B atoms, and C atoms, respectively, and *a*, *b*, and *c* are the number of A atoms, B atoms, and C atoms in an $A_aB_bC_c$ compound, respectively.

In turn, the absolute electronegativity of atoms is calculated by Equation (8) [32]:

$$\chi = 0.5(I + A) \tag{8}$$

where *I* is the ionization potential and *A* is the electron affinity (Table 4).

Table 4. The ionization potential (*I*), electron affinity (*A*), and absolute electronegativity (χ) of the Bi, W, Mo, and O atoms in the unit of "eV".

Atom	*I*	*A*	χ
Bi	7.29	0.94	4.12
W	7.98	0.82	4.40
Mo	7.10	0.75	3.93
O	13.61	1.46	7.54

Thus, the χ values for the perovskites with $x = 1$, 0.75, 0.5, 0.25, and 0 are 6.21, 6.19, 6.17, 6.15, and 6.13 eV, respectively. Figure 4 represents the calculated E_{CB} and E_{VB} values for the $Bi_2W_xMo_{1-x}O_6$ solid solutions using Equations (5) and (6).
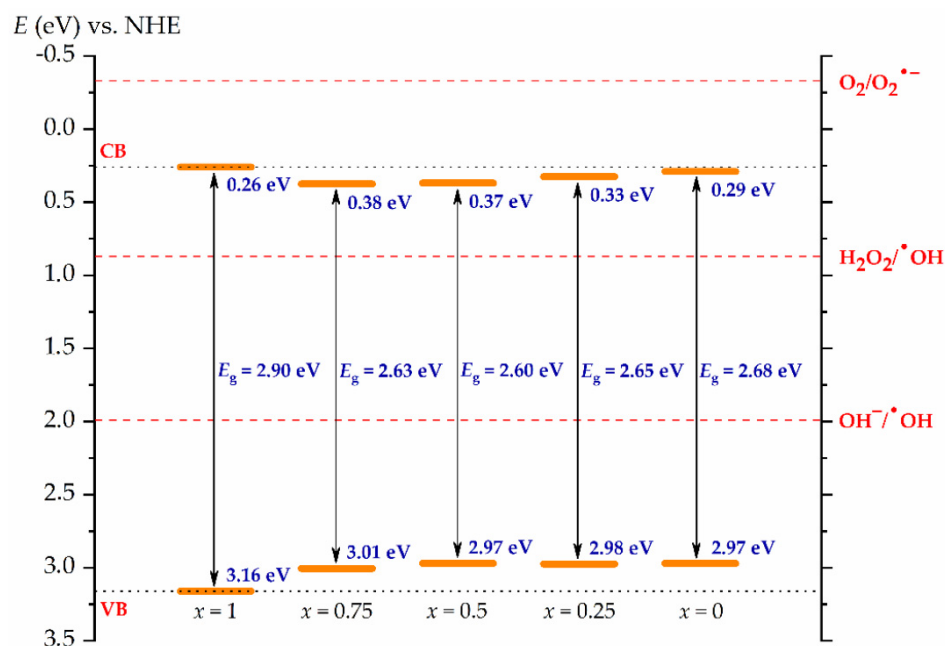

Figure 4. Calculated CB and VB edge potentials for $Bi_2W_xMo_{1-x}O_6$ solid solutions.

The energy levels of the VB maximum (VBM) and CB minimum (CBM) are the main factors in determining the redox power of photogenerated charge carriers in photocatalytic reactions. As can be seen from Figure 4, the incorporation of Mo atoms into the Bi_2WO_6 ($x = 1$) structure led to a shifting of the CB and VB edge potentials. The solid solutions with $x = 0.25$–0.5 showed a VBM upshift of 0.18–0.19 eV, while the CBM upshift was not extreme. The observed dependences are in good agreement with earlier studies [33–35], where it was demonstrated that the introduction of Mo atoms into the structure of complex oxides leads to a shifting of the CB and VB edge potentials and a narrowing of the band gap.

3.4. Photocatalytic Oxidative Desulfurization Performances

All the prepared layered perovskites $Bi_2W_xMo_{1-x}O_6$ exhibited activity in the PODS of a model mixture (200 ppm of sulfur in *n*-dodecane) under visible light irradiation

($\lambda \geq 420$ nm). To evaluate the photocatalytic activity of the materials, the conversion of DBT (or desulfurization degree) after 120 min of photocatalysis was used. As can be seen from Figure 5a, layered perovskites with $x = 0.5$–0.75 are characterized by the highest activity in PODS. It should be noted that the prepared materials can catalyze the oxidation of DBT with H_2O_2 without the light—the desulfurization degree in the dark was about 38% after 120 min in the presence of Bi_2WO_6. At the same time, the conversion of DBT was only 6% under visible light without any photocatalyst.
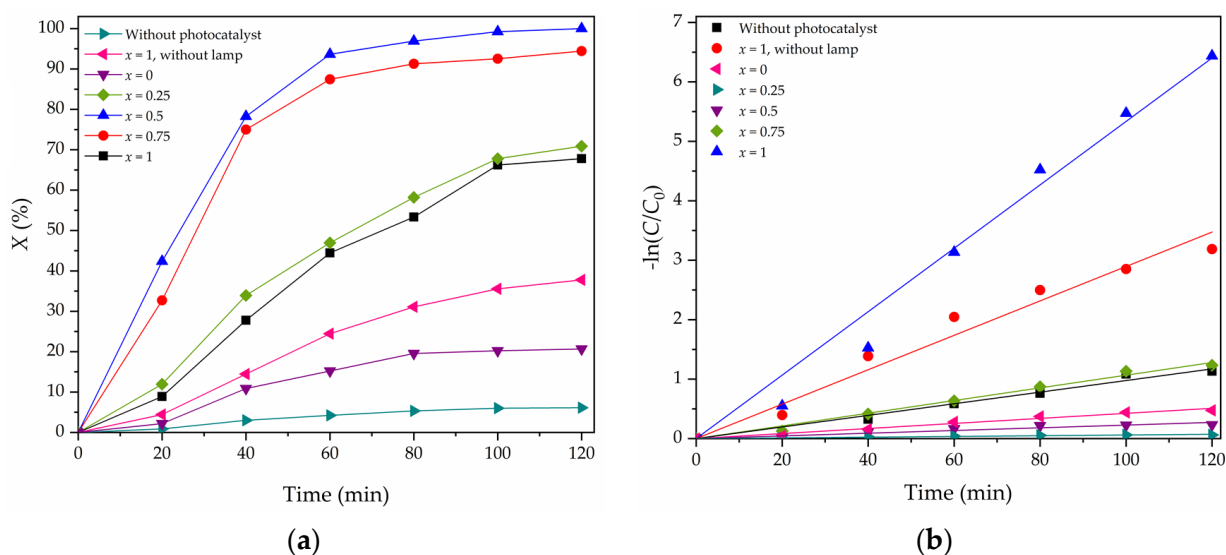

Figure 5. (**a**) Activity of perovskites $Bi_2W_xMo_{1-x}O_6$ in PODS and (**b**) pseudo-first-order kinetic fitting curves. Reaction conditions: 10 mL of model fuel, 200 ppm S, 0.1 g of photocatalyst, H_2O_2/DBT molar ratio of 10, 30 W LED lamp as the visible light source, and a distance of 10 cm from the light source to the model fuel.

The use of visible light irradiation and $Bi_2W_xMo_{1-x}O_6$ solid solutions can significantly promote the formation of •OH radicals. As a result, after 120 min of photocatalysis, the desulfurization degree was 68%, 71%, 100%, 94%, and 21% in the presence of Bi_2WO_6, $Bi_2W_{0.25}Mo_{0.75}O_6$, $Bi_2W_{0.5}Mo_{0.5}O_6$, $Bi_2W_{0.75}Mo_{0.25}O_6$, and Bi_2MoO_6, respectively. The obtained results could be considered as one of the most promising in this direction in recent years (Table 5).

Taking into account the two extreme points in the series of solid solutions, the higher photocatalytic activity of Bi_2WO_6 ($x = 1$) compared to Bi_2MoO_6 ($x = 0$) could be explained by the higher BET surface area (Table 2) and the hierarchical 3D flower-like structure of bismuth tungstate (Figure 2). On the other hand, the solid solutions with $x = 0.25$–0.75 with a lower BET surface area compared to Bi_2WO_6 are characterized by improved photocatalytic activity. This suggests that not only does the specific surface area play a significant role in the desulfurization, but also other physicochemical properties of the materials. The enhanced photocatalytic activity of the $Bi_2W_{0.25}Mo_{0.75}O_6$, $Bi_2W_{0.5}Mo_{0.5}O_6$, and $Bi_2W_{0.75}Mo_{0.25}O_6$ solid solutions is primarily attributed to their ability to absorb more visible light than Bi_2WO_6 and Bi_2MoO_6 due to a narrower band gap (Table 2). Moreover, as has been shown previously, the layered structure of perovskites [36] as well as the presence of the corner-shared [Mo/WO_6] octahedral layers may promote the generation and separation of photogenerated charges [37]. In addition, the use of the solid solutions with $x = 0.5$–0.75, which partially retain a hierarchical 3D flower-like structure, allows the complete conversion of DBT to be achieved after 120 min.

Table 5. Activity of different materials in PODS under visible light irradiation.

No. [1]	Photocatalyst	C (ppm) [2]	Oxidant	Visible Light Source	Time (min)	X (%) [3]	Main Products [4]	Ref.
1	Nb_2O_5/Bi_2WO_6	200	H_2O_2	Two 5 W LED lamps	120	99	$DBTO_2$	[18]
2	$Fe_3O_4@SiO_2/$ Bi_2WO_6/Bi_2S_3	500	Air	400 W halogen lamp	120	100	Not specified	[19]
3	$NiO-Bi_2WO_6$	200	O_2	Not specified	180	95	BTO_2	[20]
4	$CuO–Fe_3O_4$	200	H_2O_2	350 W Hg lamp	120	80	Not specified	[38]
5	$Na–g-C_3N_4$	200	O_2	300 W Xe lamp	180	35	CO_2, H_2O	[39]
6	$TiO_2@SBA-15$	50	H_2O_2	300 W Xe lamp	90	96	$DBTO_2$	[40]
7	$N–CeO_2–TiO_2$	100	H_2O_2	300 W Xe lamp	180	94	$DBTO_2$	[41]
8	$ZnO/TiO_2–SiO_2$	200	None	300 W Xe lamp	240	97	$DBTO_2$	[42]
9	$CeO_2/MIL-101(Fe)$	500	H_2O_2	500 W Xe lamp	120	90	$DBTO_2$	[43]
10	$BiOBr-C_3N_4/MCM-41$	200	H_2O_2	150 W halogen lamp	120	92	$DBTO_2$	[44]
11	$Bi_2W_{0.5}Mo_{0.5}O_6$	200	H_2O_2	30 W LED lamp	120	100	CO_2, H_2O	This study

[1] Methanol (No. 1) or acetonitrile (No. 6 and 9) were additionally added as extractants into the reaction mixture; [2] the sulfur concentration in the model fuel (DBT was used as a model organosulfur compound except in Nos. 2, 5 and 3, where thiophen and benzothiophene were used as organosulfur compounds, respectively); [3] desulfurization degree; [4] $DBTO_2$—dibenzothiophene sulfone, BTO_2—benzothiophene sulfone.

Thus, our results showed that effective PODS depends on several physicochemical properties of photocatalysts, such as absorption ability towards visible light, morphology, and BET surface area, which should always be considered together.

It should be noted that the products of incomplete oxidation of DBT, namely dibenzothiophene sulfoxide (DBTO) and dibenzothiophene sulfone ($DBTO_2$), were not detected in the reaction mass according to the GC-MS analysis. Thus, DBT was completely mineralized to CO_2 and H_2O during the reaction. At the same time, in many previous studies, it has been noted that the main oxidation product is $DBTO_2$ (Table 5). The implementation of incomplete oxidation will lead to the need for an additional of separation of the oxidation product from the hydrocarbon mixture by extraction methods [45,46].

3.5. Kinetics of PODS

The pseudo-first-order reaction was chosen in order to describe the kinetics of PODS, and the sulfur content in the model mixture should be ascribed by the following equation:

$$-\ln(C/C_0) = k \times t \tag{9}$$

where C (ppm) is the sulfur concentration within a certain period of time t, C_0 (ppm) is the initial sulfur concentration, and k is the pseudo-first-order reaction rate constant (min^{-1}).

Figure 5b represents the correlations of the time-course variation of $-\ln(C/C_0)$ versus reaction time t. It was detected that a linear increasing of $-\ln(C/C_0)$ values with the reaction time was observed for all photocatalysts, indicating the pseudo-first order. Overall, the reaction rate constants (k, min^{-1}) decrease in the following order: $Bi_2W_{0.5}Mo_{0.5}O_6$ (0.0533) > $Bi_2W_{0.75}Mo_{0.25}O_6$ (0.0289) > $Bi_2W_{0.25}Mo_{0.75}O_6$ (0.0107) > Bi_2WO_6 (0.0098) > Bi_2WO_6 without light (0.0042) > Bi_2MoO_6 (0.0022) > without any photocatalyst (0.0006). Based on the obtained results, the $Bi_2W_{0.5}Mo_{0.5}O_6$ photocatalyst was chosen for further investigations, namely for the determination of the active species role in PODS.

3.6. Active Radical Trapping

The trapping experiments were carried out by adding to the reaction mixture of IPA, BQ, and EDTA-2Na, which are scavengers of hydroxyl radicals ($^\bullet OH$), superoxide ($O_2^{\bullet -}$), and holes (h^+), respectively. As can be seen from Figure 6a, $^\bullet OH$ radicals play the

main role in the complete oxidation of DBT since the presence of IPA led to a decrease in the desulfurization degree (from 100% to 34% after 120 min over the $Bi_2W_{0.5}Mo_{0.5}O_6$ photocatalyst). The addition of other scavengers did not significantly change the DBT conversion. The crucial role of $^\bullet OH$ radicals has also been observed in the previous studies [47–49]. These conclusions are in a strong agreement with the energy diagram of the $Bi_2W_xMo_{1-x}O_6$ solid solutions (Figure 4). The formation of the superoxide radical is thermodynamically unfavorable (CBM of $Bi_2W_xMo_{1-x}O_6$ in the range of 0.26–0.38 eV, $E^0(O_2/O_2^{\bullet-}) = -0.33$ eV). On the other hand, $^\bullet OH$ can be generated because the CB position of $Bi_2W_xMo_{1-x}O_6$ is higher than $E^0(H_2O_2/^\bullet OH) = 0.87$ eV [50,51]. According to these results, the photocatalytic mechanism was put forward (Figure 6b).
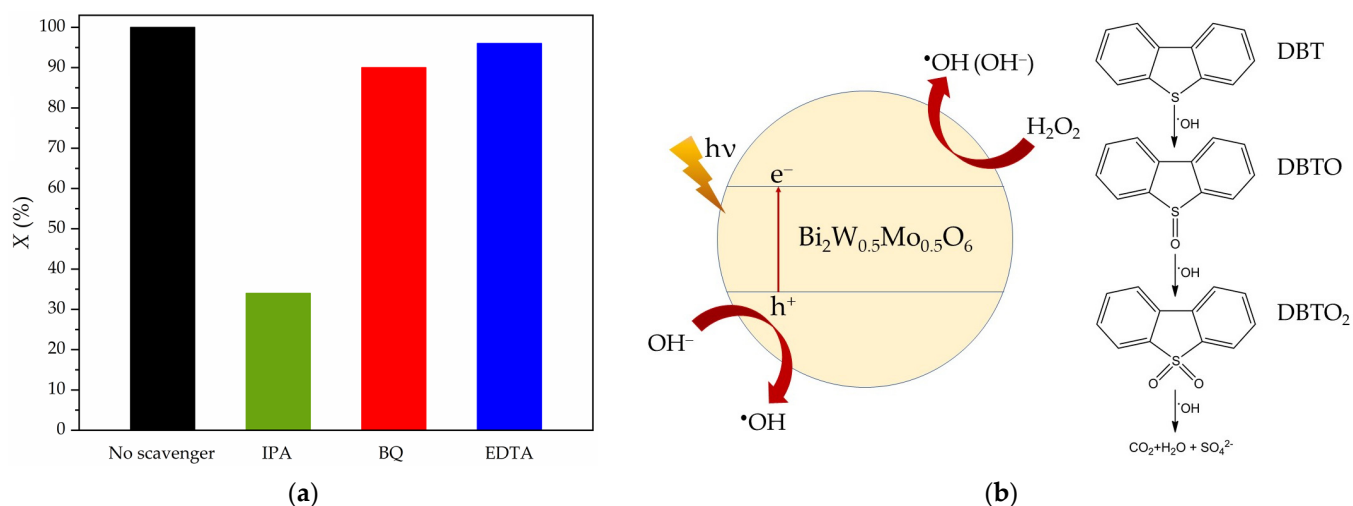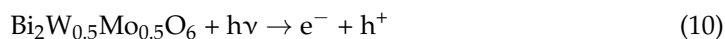

Figure 6. (**a**) Desulfurization degree after 120 min in the presence of free radical scavengers (10 mL of model fuel, 200 ppm S, 0.1 g of $Bi_2W_{0.5}Mo_{0.5}O_6$ photocatalyst, H_2O_2/DBT molar ratio of 10, 30 W LED lamp as the visible light source, a distance of 10 cm from the light source to the model fuel) and (**b**) possible mechanism of photocatalytic oxidation of DBT on $Bi_2W_{0.5}Mo_{0.5}O_6$.

During the photocatalytic process, the $Bi_2W_{0.5}Mo_{0.5}O_6$ photocatalyst can be activated under visible light irradiation (Equation (10)). The photogenerated electrons (e^-) react with H_2O_2 to form $^\bullet OH$ radicals (Equation (11)). In addition, the photogenerated holes (h^+) can oxidize OH^- with the formation of $^\bullet OH$ radicals (Equation (12)). The oxidation of the DBT molecule occurs due to $^\bullet OH$ radicals, which are characterized by a strong oxidation ability (Equation (13)).

$$Bi_2W_{0.5}Mo_{0.5}O_6 + h\nu \rightarrow e^- + h^+ \tag{10}$$

$$e^- + H_2O_2 \rightarrow {}^\bullet OH + OH^- \tag{11}$$

$$h^+ + OH^- \rightarrow {}^\bullet OH \tag{12}$$

$$DBT + {}^\bullet OH \rightarrow CO_2 + H_2O + SO_4{}^{2-} \tag{13}$$

3.7. Stability and Recycling Performance of the Photocatalyst

The stability of the photocatalyst is an important factor which determines the possibility of the practical application of the developed photocatalytic materials. Accordingly, the stability of the $Bi_2W_{0.5}Mo_{0.5}O_6$ photocatalyst was studied through reusability experiments. As shown in Figure 7, the desulfurization degree was high and exceeded 90% after five cycles of PODS. A slight decrease in the conversion of DBT could be explained by agglomeration of the photocatalyst particles during PODS.
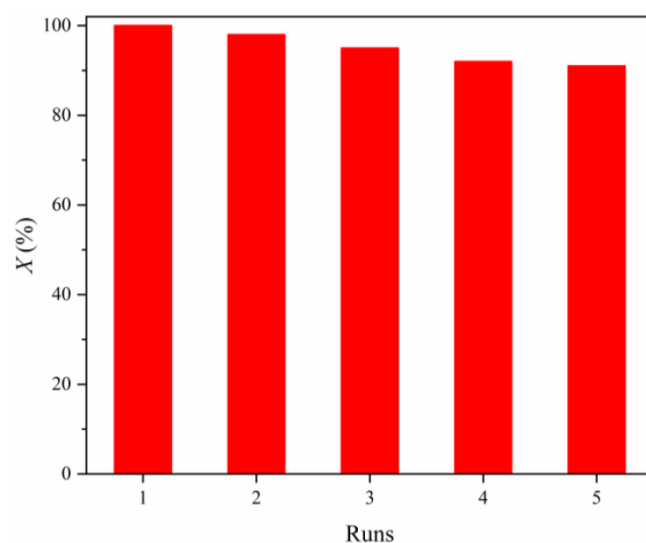
Figure 7. Reusability of $Bi_2W_{0.5}Mo_{0.5}O_6$ photocatalyst. Reaction conditions: 10 mL of model fuel, 200 ppm S, 0.1 g of photocatalyst, H_2O_2/DBT molar ratio of 10, 30 W LED lamp as the visible light source, and a distance of 10 cm from the light source to the model fuel.

3.8. Future Research Directions

We also assume that $Bi_2W_xMo_{1-x}O_6@Bi_2MoO_6$ or $Bi_2W_xMo_{1-x}O_6@Bi_2WO_6$ heterojunctions may be formed in $Bi_2W_xMo_{1-x}O_6$ solid solutions. The formation of heterojunctions in materials promotes an efficient spatial separation of charge carriers. However, this assumption requires careful investigation in order to establish the real mechanism of reactions during PODS in the presence of the $Bi_2W_xMo_{1-x}O_6$ solid solutions. Thus, the identification of heterojunctions formed during the preparation of $Bi_2W_xMo_{1-x}O_6$ could be the subject of further research.

We suppose that further increasing of the photocatalytic activity of these types of materials in PODS could be achieved by the optimization of the synthesis conditions in order to find the most appropriate morphology. It is known that a well-designed structure allows the separation of photogenerated charges and efficient light adsorption to be achieved, taking full advantage of the reflection, refraction, and scattering of photons [52]. It has been demonstrated that modulating reaction temperature, reaction time, and pH value, and changing the surfactant and template during hydrothermal treatment can be efficient for the preparation of Bi_2WO_6 with different morphologies, such as erythrocyte-like [53], flower-like [54], single-crystal-like [55], and 3D hollow [56]. Also, varying the preparation conditions affects the physicochemical properties of the obtained materials (e.g., specific surface area and band gap) [57], which significantly influences the photocatalytic performances. Thus, the second subject of further research in this direction could be the search for the optimal preparation conditions of the solid solutions.

4. Conclusions

In summary, nanosized $Bi_2W_xMo_{1-x}O_6$ solid solutions with various compositions (x = 1, 0.75, 0.5, 0.25, 0) were prepared by a hydrothermal method. The incorporation of Mo into the Bi_2WO_6 lattice leads to the $Bi_2W_xMo_{1-x}O_6$ solid solutions (x = 0.75, 0.5, 0.25), which are characterized by a narrowed band gap and enhanced visible light-harvesting ability. The solid solutions with x = 0.5–0.75 partially retain a hierarchical 3D flower-like structure, and their use in PODS allows the complete conversion of DBT to be achieved after 120 min. The obtained results confirmed that the physicochemical properties of photocatalysts, such as visible light absorption ability, morphology, and BET surface area, have a significant influence on the reaction and should be considered together for the efficient realization of PODS. In addition, the trapping experiments showed that the sulfur removal proceeds due to $^\bullet OH$ radicals. We also suggested directions for further research, namely optimization of

the preparation conditions of the solid solutions and the identification of heterojunctions formed during the preparation of $Bi_2W_xMo_{1-x}O_6$.

References

1.　Yang, X.; Wang, D. Photocatalysis: From fundamental principles to materials and applications. *ACS Appl. Energy Mater.* **2018**, *1*, 6657–6693. [CrossRef]

2.　Hitam, C.N.C.; Jalil, A.A.; Abdulrasheed, A.A. A review on recent progression of photocatalytic desulphurization study over decorated photocatalysts. *J. Ind. Eng. Chem.* **2019**, *74*, 172–186. [CrossRef]

3.　Zhou, X.; Wang, T.; Liu, H.; Gao, X.; Wang, C.; Wang, G. Desulfurization through photocatalytic oxidation: A critical review. *ChemSusChem* **2020**, *14*, 492–511. [CrossRef]

4.　Li, K.; An, X.; Park, K.H.; Khraisheh, M.; Tang, J. A critical review of CO_2 photoconversion: Catalysts and reactors. *Catal. Today* **2014**, *224*, 3–12. [CrossRef]

5.　Jitan, S.A.; Palmisano, G.; Garlisi, C. Synthesis and surface modification of TiO_2-based photocatalysts for the conversion of CO_2. *Catalysts* **2020**, *10*, 227. [CrossRef]

6.　Belousov, A.S.; Suleimanov, E.V. Application of metal–organic frameworks as an alternative to metal oxide-based photocatalysts for the production of industrially important organic chemicals. *Green Chem.* **2021**, *23*, 6172–6204. [CrossRef]

7.　Chen, Y.; Shen, C.; Wang, J.; Xiao, G.; Luo, G. Green synthesis of Ag–TiO_2 supported on porous glass with enhanced photo-catalytic performance for oxidative desulfurization and removal of dyes under visible light. *ACS Sustain. Chem. Eng.* **2018**, *6*, 13276–13286. [CrossRef]

8.　Zhang, G.; Gao, M.; Tian, M.; Zhao, W. In situ hydrothermal preparation and photocatalytic desulfurization performance of graphene wrapped TiO_2 composites. *J. Solid State Chem.* **2019**, *279*, 120953. [CrossRef]

9.　Man, Z.; Meng, Y.; Lin, X.; Dai, X.; Wang, L.; Liu, D. Assembling UiO-66@TiO_2 nanocomposites for efficient photocatalytic degradation of dimethyl sulfide. *Chem. Eng. J.* **2022**, *431*, 133952. [CrossRef]

10.　Wang, L.; Ma, Y.; Xie, D.; Zhang, M.; Zuo, N.; Mominou, N.; Jing, C. Ultra-deep desulfurization of model diesel fuel over Pr/Ce–N–TiO_2 assisted by visible light. *Microporous Mesoporous Mater.* **2021**, *323*, 111258. [CrossRef]

11.　Ortiz-Bustos, J.; Hierro, I.; Pérez, Y. Photocatalytic oxidative desulfurization and degradation of organic pollutants under visible light using TiO_2 nanoparticles modified with iron and sulphate ions. *Ceram. Int.* **2022**, *48*, 6905–6916. [CrossRef]

12.　Qin, Y.; Li, H.; Ding, Y.; Ma, C.; Liu, X.; Meng, M.; Yan, Y. Fabrication of Bi_2WO_6/In_2O_3 photocatalysts with efficient photocatalytic performance for the degradation of organic pollutants: Insight into the role of oxygen vacancy and heterojunction. *Adv. Powder Technol.* **2020**, *31*, 2890–2900. [CrossRef]

13.　Orimolade, B.O.; Idris, A.O.; Feleni, U.; Mamba, B. Recent advances in degradation of pharmaceuticals using Bi_2WO_6 mediated photocatalysis–A comprehensive review. *Environ. Pollut.* **2021**, *289*, 117891. [CrossRef] [PubMed]

14.　Nie, H.; Wei, K.; Li, Y.; Liu, Y.; Zhao, Y.; Huang, H.; Shao, M.; Liu, Y.; Kang, Z. Carbon dots/Bi_2WO_6 composite with compensatory photo-electronic effect for overall water photo-splitting at normal pressure. *Chin. Chem. Lett.* **2021**, *32*, 2283–2286. [CrossRef]

15.　Chen, P.; Du, T.; Jia, H.; Zhou, L.; Yue, Q.; Wang, H.; Wang, Y. A novel Bi_2WO_6/Si heterostructure photocatalyst with Fermi level shift in valence band realizes efficient reduction of CO_2 under visible light. *Appl. Surf. Sci.* **2022**, *585*, 152665. [CrossRef]

16.　Liu, X.; Gu, S.; Zhao, Y.; Zhou, G.; Li, W. $BiVO_4$, Bi_2WO_6 and Bi_2MoO_6 photocatalysis: A brief review. *J. Mater. Sci. Technol.* **2020**, *56*, 45–68. [CrossRef]

17.　Chen, T.; Liu, L.; Hu, C.; Huang, H. Recent advances on Bi_2WO_6-based photocatalysts for environmental and energy applications. *Chin. J. Catal.* **2021**, *42*, 1413–1438. [CrossRef]

18.　Wu, J.; Li, J.; Liu, J.; Bai, J.; Yang, L. A novel Nb_2O_5/Bi_2WO_6 heterojunction photocatalytic oxidative desulfurization catalyst with high visible light-induced photocatalytic activity. *RSC Adv.* **2017**, *7*, 51046–51054. [CrossRef]

19. Guo, L.; Zhao, Q.; Wang, C.; Shen, H.; Han, X.; Zhang, K.; Wang, D.; Fu, F. Magnetically recyclable $Fe_3O_4@SiO_2/Bi_2WO_6/Bi_2S_3$ with visible-light-driven photocatalytic oxidative desulfurization. *Mater. Res. Bull.* **2019**, *118*, 110520. [CrossRef]

20. Chang, H.; Yi, H.; Zhang, J. Preparation of a $NiO-Bi_2WO_6$ catalyst and its photocatalytic oxidative desulfurization performance. *Colloid Interface Sci. Commun.* **2021**, *41*, 100381. [CrossRef]

21. Li, X.; Li, F.; Lu, X.; Zuo, S.; Yao, C.; Ni, C. Development of $Bi_2W_{1−x}Mo_xO_6$/montmorillonite nanocomposite as efficient catalyst for photocatalytic desulfurization. *J. Alloys Compd.* **2017**, *709*, 285–292. [CrossRef]

22. Tauc, J.; Grigorovici, R.; Vancu, A. Optical properties and electronic structure of amorphous germanium. *Phys. Status Solidi* **1966**, *15*, 627–637. [CrossRef]

23. Wang, H.; Song, J.; Zhang, H.; Gao, F.; Zhao, S.; Hu, H. Controlled synthesis of three-dimensional hierarchical Bi_2WO_6 microspheres with optimum photocatalytic activity. *Mater. Res. Bull.* **2012**, *47*, 315–320. [CrossRef]

24. Li, G. Electrospinning fabrication and photocatalytic activity of Bi_2WO_6 nanofibers. *J. Mater. Sci. Mater. Electron.* **2017**, *28*, 12320–12325. [CrossRef]

25. Sun, Y.; Wang, W.; Sun, S.; Zhang, L. A general synthesis strategy for one-dimensional Bi_2MO_6 (M = Mo, W) photocatalysts using an electrospinning method. *CrystEngComm* **2013**, *15*, 7959–7964. [CrossRef]

26. Voronkova, V.I.; Kharitonova, E.P.; Rudnitskaya, O.G. Refinement of Bi_2WO_6 and Bi_2MoO_6 polymorphism. *J. Alloys Compd.* **2009**, *487*, 274–279. [CrossRef]

27. Zhang, J.; Deng, P.; Deng, M.; Shen, H.; Feng, Z.; Li, H. Hybrid density functional theory study of native defects and nonmetal (C, N, S, and P) doping in a Bi2WO6 photocatalyst. *ACS Omega* **2020**, *5*, 29081–29091. [CrossRef]

28. Mulliken, R.S. A new electroaffinity scale; together with data on valence states and on valence ionization potentials and electron affinities. *J. Chem. Phys.* **1934**, *2*, 782–793. [CrossRef]

29. Mulliken, R.S. Electronic structures of molecules XI. Electroaffinity, molecular orbitals and dipole moments. *J. Chem. Phys.* **1935**, *3*, 573–585. [CrossRef]

30. Halouani, F.E.; Deschanvres, A. Interfaces semi-conducteur-electrolyte: Correlations entre le potentiel de bande plate et les echelles d'electronegativite. *Mater. Res. Bull.* **1982**, *17*, 1045–1052. [CrossRef]

31. Gao, J.; Zeng, W.; Tang, B.; Zhong, M.; Liu, Q.-J. Density functional characterization of Bi-based photocatalysts: $BiTaO_4$, $Bi_4Ta_2O_{11}$ and $Bi_7Ta_3O_{18}$. *Mater. Sci. Semicond. Process.* **2021**, *121*, 105447. [CrossRef]

32. Pearson, R.G. Absolute electronegativity and absolute hardness of Lewis acids and bases. *J. Am. Chem. Soc.* **1985**, *107*, 6801–6806. [CrossRef]

33. Zhou, L.; Yu, M.; Yang, J.; Wang, Y.; Yu, C. Nanosheet-based $Bi_2Mo_xW_{1−x}O_6$ solid solutions with adjustable band gaps and enhanced visible-light-driven photocatalytic activities. *J. Phys. Chem. C* **2010**, *114*, 18812–18818. [CrossRef]

34. Schwertmann, L.; Grünert, A.; Pougin, A.; Sun, C.; Wark, M.; Marschall, R. Understanding the influence of lattice composition on the photocatalytic activity of defect-pyrochlore-structured semiconductor mixed oxides. *Adv. Funct. Mater.* **2015**, *25*, 905–912. [CrossRef]

35. Xie, Y.; Liu, D.; Wang, B.; Li, D.; Yan, Z.; Chen, Y.; Shen, J.; Zhang, Z.; Wang, X. Monolayer $Bi_2W_{1−x}Mo_xO_6$ solid solutions for structural polarity to boost photocatalytic reduction of nitrobenzene under visible light. *ACS Sustain. Chem. Eng.* **2021**, *9*, 2465–2474. [CrossRef]

36. Hu, Y.; Mao, L.; Guan, X.; Tucker, K.A.; Xie, H.; Wu, X.; Shi, J. Layered perovskite oxides and their derivative nanosheets adopting different modification strategies towards better photocatalytic performance of water splitting. *Renew. Sustain. Energy Rev.* **2020**, *119*, 109527. [CrossRef]

37. Fu, H.; Zhang, L.; Yao, W.; Zhu, Y. Photocatalytic properties of nanosized Bi_2WO_6 catalysts synthesized via a hydrothermal process. *Appl. Catal. B* **2006**, *66*, 100–110. [CrossRef]

38. Ammar, S.H.; Kareem, Y.S.; Ali, A.D. Photocatalytic oxidative desulfurization of liquid petroleum fuels using magnetic CuO–Fe_3O_4 nanocomposites. *J. Environ. Chem. Eng.* **2018**, *6*, 6780–6787. [CrossRef]

39. Zhang, X.; Song, H.; Sun, C.; Chen, C.; Han, F.; Li, X. Photocatalytic oxidative desulfurization and denitrogenation of fuels over sodium doped graphitic carbon nitride nanosheets under visible light irradiation. *Mater. Chem. Phys.* **2019**, *226*, 34–43. [CrossRef]

40. Guo, G.; Guo, H.; Wang, F.; France, L.J.; Yang, W.; Mei, Z.; Yu, Y. Dye-sensitized TiO_2@SBA-15 composites: Preparation and their application in photocatalytic desulfurization. *Green Energy Environ.* **2020**, *5*, 114–120. [CrossRef]

41. Lu, X.; Li, X.; Chen, F.; Chen, Z.; Qian, J.; Zhang, Q. Biotemplating synthesis of N-doped two-dimensional $CeO_2–TiO_2$ nanosheets with enhanced visible light photocatalytic desulfurization performance. *J. Alloys Compd.* **2020**, *815*, 152326. [CrossRef]

42. Zhou, K.; Ding, Y.; Zhang, L.; Wu, H.; Guo, J. Synthesis of mesoporous $ZnO/TiO_2–SiO_2$ composite material and its application in photocatalytic adsorption desulfurization without the addition of an extra oxidant. *Dalton Trans.* **2020**, *49*, 1600–1612. [CrossRef] [PubMed]

43. Huo, Q.; Liu, G.; Sun, H.; Fu, Y.; Ning, Y.; Zhang, B.; Zhang, X.; Gao, J.; Miao, J.; Zhang, X.; et al. CeO_2-modified MIL-101(Fe) for photocatalysis extraction oxidation desulfurization of model oil under visible light irradiation. *Chem. Eng. J.* **2021**, *422*, 130036. [CrossRef]

44. Abedini, F.; Allahyari, S.; Rahemi, N. Oxidative desulfurization of dibenzothiophene and simultaneous adsorption of products on $BiOBr-C_3N_4$/MCM-41 visible-light-driven core–shell nano photocatalyst. *Appl. Surf. Sci.* **2021**, *569*, 151086. [CrossRef]

45. Majid, M.F.; Zaid, H.F.M.; Kait, C.F.; Jumbri, K.; Yuan, L.C.; Rajasuriyan, S. Futuristic advance and perspective of deep eutectic solvent for extractive desulfurization of fuel oil: A review. *J. Mol. Liq.* **2020**, *306*, 112870. [CrossRef]

46. Tahir, S.; Qazi, U.Y.; Naseem, Z.; Tahir, N.; Zahid, M.; Javaid, R.; Shahid, I. Deep eutectic solvents as alternative green solvents for the efficient desulfurization of liquid fuel: A comprehensive review. *Fuel* **2021**, *305*, 121502. [CrossRef]

47. Mandizadeh, S.; Salavati-Niasari, M.; Sadri, M. Hydrothermal synthesis, characterization and magnetic properties of $BaFe_2O_4$ nanostructure as a photocatalytic oxidative desulfurization of dibenzothiophene. *Sep. Purif. Technol.* **2017**, *175*, 399–405. [CrossRef]

48. Pham, X.N.; Nguyen, M.B.; Ngo, H.S.; Doan, H.V. Highly efficient photocatalytic oxidative desulfurization of dibenzothiophene with sunlight irradiation using green catalyst of Ag@AgBr/Al-SBA-15 derived from natural halloysite. *J. Ind. Eng. Chem.* **2020**, *90*, 358–370. [CrossRef]

49. Lu, X.; Chen, F.; Qian, J.; Fu, M.; Jiang, Q.; Zhang, Q. Facile fabrication of CeF_3/g-C_3N_4 heterojunction photocatalysts with upconversion properties for enhanced photocatalytic desulfurization performance. *J. Rare Earths* **2021**, *39*, 1204–1210. [CrossRef]

50. Deng, F.; Lu, X.; Pei, X.; Luo, X.; Luo, S.; Dionysiou, D.D. Fabrication of ternary reduced graphene oxide/SnS_2/$ZnFe_2O_4$ composite for high visible-light photocatalytic activity and stability. *J. Hazard. Mater.* **2017**, *332*, 149–161. [CrossRef]

51. Cao, Y.; Ren, Y.; Zhang, J.; Xie, T.; Lin, Y. Activation of H_2O_2 by photo-generated electrons for enhanced visible light driven methylene blue degradation with $ZnFe_2O_4$/$BiVO_4$ heterojunction. *Opt. Mater.* **2021**, *121*, 111637. [CrossRef]

52. Belousov, A.S.; Suleimanov, E.V.; Fukina, D.G. Pyrochlore oxides as visible light-responsive photocatalysts. *New J. Chem.* **2021**, *45*, 22531–22558. [CrossRef]

53. Li, C.; Chen, G.; Sun, J.; Feng, Y.; Liu, J.; Dong, H. Ultrathin nanoflakes constructed erythrocyte-like Bi_2WO_6 hierarchical architecture via anionic self-regulation strategy for improving photocatalytic activity and gas-sensing property. *Appl. Catal. B* **2015**, *163*, 415–423. [CrossRef]

54. Liu, Y.; Chen, L.; Yuan, Q.; He, J.; Au, C.-T.; Yin, S.-F. A green and efficient photocatalytic route for the highly-selective oxidation of saturated alpha-carbon C–H bonds in aromatic alkanes over flower-like Bi_2WO_6. *Chem. Commun.* **2016**, *52*, 1274–1277. [CrossRef]

55. Li, C.; Chen, G.; Sun, J.; Rao, J.; Han, Z.; Hu, Y.; Zhou, Y. A novel mesoporous single-crystal-like Bi_2WO_6 with enhanced photocatalytic activity for pollutants degradation and oxygen production. *ACS Appl. Mater. Interfaces* **2015**, *7*, 25716–25724. [CrossRef]

56. Chen, M.; Huang, Y.; Lee, S.C. Salt-assisted synthesis of hollow Bi_2WO_6 microspheres with superior photocatalytic activity for NO removal. *Chin. J. Catal.* **2017**, *38*, 348–356. [CrossRef]

57. Nagyné-Kovács, T.; Shahnazarova, G.; Lukács, I.E.; Szabó, A.; Hernadi, K.; Igricz, T.; László, K.; Szilágyi, I.M.; Pokol, G. Effect of pH in the hydrothermal preparation of Bi_2WO_6 nanostructures. *Materials* **2019**, *12*, 1728. [CrossRef]